


ORIGINAL ARTICLE

Open Access



# Atomic construction and spectroscopic characterization of FeSe-derived thin films on SrTiO<sub>3</sub> substrates

Yao Zhang<sup>1</sup>, Zhi-Mo Zhang<sup>1</sup>, Jin-Hua Nie<sup>1</sup>, Wenhao Zhang<sup>1\*</sup>  and Ying-Shuang Fu<sup>1\*</sup>

## Abstract

Controllably fabricating low-dimensional systems and unraveling their exotic states at the atomic scale is a pivotal step for the construction of quantum functional materials with emergent states. Here, by utilizing the elaborated molecular beam epitaxy growth, we obtain various Fe<sub>x</sub>Se<sub>y</sub> phases beyond the single-layer FeSe/SrTiO<sub>3</sub> films. A synthetic strategy of lowering substrate temperature with superfluous Se annealing is implemented to achieve various stoichiometric FeSe-derived phases, ranging from 1:1 to 5:8. The phase transitions and electronic structure of these Fe<sub>x</sub>Se<sub>y</sub> phases are systematically characterized by atomic resolution scanning tunneling microscopy measurements. We observe the long-ranged antiferromagnetic order of the Fe<sub>4</sub>Se<sub>5</sub> phase by spin-polarized signals with striped patterns, which is also verified by their magnetic response of phase shift between adjacent domains. The electronic doping effect in insulating Fe<sub>4</sub>Se<sub>5</sub> and the kagome effect in metallic Fe<sub>5</sub>Se<sub>8</sub> are also discussed, where the kagome lattice is a promising structure to manifest both spin frustration of d electrons in a quantum-spin-liquid phase and correlated topological states with flat-band physics. Our study provides promising opportunities for constructing artificial superstructures with tunable building blocks, which is helpful for understanding the emergent quantum states and their correlation with competing orders in the FeSe-based family.

**Keywords** FeSe-derived films, Molecular beam epitaxy, Scanning tunneling microscopy, Antiferromagnetic stripes, Surface doping, Kagome lattice

## 1 Introduction

In analogy to the unconventional superconductors of cuprates and iron pnictides, interface-enhanced high-transition temperature (high-T<sub>C</sub>) superconductivity in single-layer FeSe films on SrTiO<sub>3</sub> has boomed an upsurge in a great deal of attractable interest in the condensed-matter community [1–5], including the unusual interfacial effect, the underlying pairing mechanism, the

magnetic ground states and other competing orders. Till now, some degree of consensus has been reached on the origin of T<sub>C</sub> enhancement, ascribing to a combination of two major contributing factors—the interface-induced channel (tensile strain [6–9] and electron-phonon coupling [3, 10–12]) and electron doping effect [13–16]. Meanwhile, there emerge extensive explorations concerning the electron phase diagram [16–18], electron pairing symmetries [19–22], electron-phonon coupling [23–25], pre-formed pairing of Cooper pairs and pseudogap behavior [26–28], etc.

Among these debates, searching for other FeSe-derived compounds, associated with their relationship to single-layer FeSe/SrTiO<sub>3</sub> films, may be a plausible route to understanding the mystery of unconventional mechanisms and interfacial enhancement in

\*Correspondence:

Wenhao Zhang  
wenhaozhang@hust.edu.cn  
Ying-Shuang Fu  
yfu@hust.edu.cn

<sup>1</sup> School of Physics and Wuhan National High Magnetic Field Center, Huazhong University of Science and Technology, Wuhan 430074, China



© The Author(s) 2023. **Open Access** This article is licensed under a Creative Commons Attribution 4.0 International License, which permits use, sharing, adaptation, distribution and reproduction in any medium or format, as long as you give appropriate credit to the original author(s) and the source, provide a link to the Creative Commons licence, and indicate if changes were made. The images or other third party material in this article are included in the article's Creative Commons licence, unless indicated otherwise in a credit line to the material. If material is not included in the article's Creative Commons licence and your intended use is not permitted by statutory regulation or exceeds the permitted use, you will need to obtain permission directly from the copyright holder. To view a copy of this licence, visit <http://creativecommons.org/licenses/by/4.0/>.

superconductivity. For instance, both transport and ARPES experiments argued that the Fe-vacancy ordered  $\text{Fe}_4\text{Se}_5$  [29, 30] (or undoped  $\text{FeSe}/\text{SrTiO}_3$  films [31]) should be the insulating parent phase of  $\text{FeSe}$  (or  $\text{FeSe}/\text{SrTiO}_3$ ). In particular, the  $\text{Fe}_4\text{Se}_5$  phase is manifested as a Mott insulator possessing a block-checkerboard antiferromagnetic (AFM) order, resembling the  $\text{A}_2\text{Fe}_4\text{Se}_5$  compounds ( $\text{A} = \text{K}, \text{Tl}, \text{Rb}, \text{or Cs}$ ) [32, 33]. Such similarity between  $\text{A}_{1-x}\text{Fe}_{2-y}\text{Se}_2$  and  $\text{FeSe}/\text{SrTiO}_3$  films is also consistent with the dramatic  $T_C$  enhancement of  $\text{FeSe}$  superconductor by heavy electron doping [15, 34, 35]. Also, there report a large amount of  $\text{FeSe}$ -based superconductors by intercalation of organic molecules or inorganic elements, such as  $\text{Li}_x(\text{NH}_2)_y(\text{NH}_3)_{1-y}\text{Fe}_2\text{Se}_2$  [36],  $(\text{Li}_{0.8}\text{Fe}_{0.2})\text{OHFeSe}$  [37],  $(\text{CTA})_{0.3}\text{FeSe}$  [38]. Different from the wet-chemical synthesis of liquid-ammonia and electrochemical methods, molecular beam epitaxy (MBE) is a liquid-free and controllable growth to gain different constituents of  $\text{FeSe}$  with high quality of atomically flat thin films, as well as investigating their complex phase transitions. Previously, we have also actualized the MBE-controlled synthesis on the multiple phases of the sister  $\text{Fe}-\text{Te}$  compound with three structural phases:  $\alpha\text{-FeTe}$ ,  $\beta\text{-FeTe}$ , and  $\text{FeTe}_2$  of different intersections [39]. Other  $\text{FeSe}_x$  phases are sporadically reported [40, 41]; however, there is still a lack of a concordant growth scenario for the  $\text{FeSe}$ -derived thin films.

In this study, we report a compositive route to synthesize distinct  $\text{Fe}_x\text{Se}_y$  phases based on the single-layer  $\text{FeSe}/\text{SrTiO}_3$  films via MBE growth. The key essentials lie in the elaborate control of supplying excess Se flux and low-temperature annealing treatment. Various stoichiometries of  $\text{FeSe}$ -derived compounds are synthesized with atomically smooth surfaces and largely flat terraces, including  $\alpha\text{-FeSe}$ ,  $\beta\text{-FeSe}$ ,  $\text{Fe}_3\text{Se}_4$ ,  $\text{Fe}_4\text{Se}_5$ ,  $\text{Fe}_5\text{Se}_6$ ,  $\text{Fe}_6\text{Se}_7$ , and  $\text{Fe}_5\text{Se}_8$ . While  $\text{Fe}_4\text{Se}_5$ ,  $\text{Fe}_5\text{Se}_6$ , and  $\text{Fe}_6\text{Se}_7$  are distinguished by different densities of ordered Fe vacancies,  $\text{Fe}_3\text{Se}_4$  and  $\text{Fe}_5\text{Se}_8$  are constructed by selective intercalations of Fe atoms. Scanning tunneling microscopy/spectroscopy (STM/STS) measurements are used to reveal the structural characteristics, electronic properties, and phase transitions among these  $\text{Fe}_x\text{Se}_y$  phases. Specifically,  $\text{Fe}_4\text{Se}_5$  exhibits an in-plane AFM order with unidirectional stripes as real-space spin contrasts, which is sustained by the magnetic response of AFM domains. We also discuss the electronic doping effect in insulating  $\text{Fe}_4\text{Se}_5$  by surface K dosing, which seems inadequate to drive  $\text{Fe}_4\text{Se}_5$  into the superconducting regime. Our MBE implication of fabricating different stoichiometries of  $\text{Fe}_x\text{Se}_y$  phases sheds light on constructing and transforming  $\text{FeSe}$ -related families, ranging from 3D to 2D systems, which

is expected to be an appealing platform to create and tune potentially exotic states in the extensive library of quantum materials.

## 2 Experiments and methods

All  $\text{Fe}_x\text{Se}_y$  thin samples were prepared by the MBE method in a customized ultrahigh vacuum chamber at a base pressure of  $5 \times 10^{-10}$  mbar [42]. Before growth, the atomically flat Nb-doped  $\text{SrTiO}_3(001)$  substrate (0.7 wt %) was obtained by (1) degassing at 873 K for 2 h, (2) thermally heated to  $\sim 1223$  K with a Se flux for half an hour, (3) flashed to 1320 K for an hour. High-purity Fe (powder, 99.99%; Alfa Aesar) and Se sources (shot, 99.9999%; Alfa Aesar) were used for co-evaporating from standard K cells. During the growth process, the Fe flux was fixed at 1370 K, giving a growth rate of  $\sim 0.2$  monolayer/min. The Se/Fe flux ratio was adjusted by precisely varying the temperature of the Se source. The substrate temperature was controlled by direct current heating, which was monitored by an infrared pyrometer.

As a starting point, epitaxial  $\beta\text{-FeSe}/\text{SrTiO}_3$  films were first fabricated, with the substrate holding at 673 K [2]. It can become superconducting by annealing to 773 K for 2 h [14]. The hexagonal  $\alpha\text{-FeSe}$  phase was obtained by annealing  $\beta\text{-FeSe}$  at 473 K for 1 h. Variant Fe-vacancy phases were achieved by gently annealing the as-grown sample at 373–423 K with a Se overflux for 30 min to 2 h. The K deposition was performed in situ at a temperature of 20–50 K by using a potassium dispenser (SAES Getters). The coverage of K adatoms is accumulated by repeated depositions onto the  $\text{Fe}_x\text{Se}_y/\text{SrTiO}_3$  surface, with 10–30 s in each cycle [43].

The low-temperature STM/STS measurements were conducted on a commercial STM system (Unisoku-1500) at a base temperature of 2 K [44]. W tip was electrochemically etched and then cleaned by e-beam at  $\sim 1900$  K to remove its apex oxides, which were calibrated on a standard  $\text{Ag}(111)$  sample prior to STM measurements. All topographic images were taken in a constant-current mode, and the tunneling spectra and conductance mappings were acquired by a standard lock-in technique with a modulation voltage ( $V_{\text{mod}}$ ) at 983 Hz [45]. The spin-polarized STM (SP-STM) measurements were carried out by using a spin-polarized Fe-coated W tip, which was fabricated by depositing  $\sim 20$  nm Fe clusters onto the apex of the calibrated W tip, followed by annealing at  $\sim 500$  K for 10 min. The spin-polarized properties of the Fe-coated tip were verified by mapping the zigzag patterns on an AFM  $\text{CrTe}_2$  surface [46]. An external magnetic field was applied perpendicular to the surface of  $\text{FeSe}/\text{SrTiO}_3$  films.

### 3 Results and discussion

The formation of different  $\text{Fe}_x\text{Se}_y$  phases is achieved by the precise combination of (i) controlling the substrate temperature, (ii) adjusting the Se/Fe ratio, and (iii) post-annealing under Se flux, as illustrated in Fig. 1a. Firstly, we start from the easily obtained  $\beta$ -FeSe films by the mature process as reported [2, 14]. On the one hand, it can convert to  $\alpha$ -FeSe thin films by annealing at a low temperature of  $\sim 473$  K, with the typical STM morphology shown in Fig. 1b. Obviously, the islands are triangle-shaped with large terraces of atomically smooth Se-terminated surface, indicating a phase transition from tetragonal  $\beta$ -FeSe (layered) into hexagonal  $\alpha$ -FeSe (nonlayered). Their high-resolution STM images associated with their crystalline structural models are shown in Fig. 2a, b. On the other hand, by gradually increasing the Se flux, we can obtain various ordered phases from  $\beta$ -FeSe. As reported in our previous study [47], the distinct superstructures of  $\sqrt{5} \times \sqrt{10}$  (1/7 Fe vacancies or  $\text{Fe}_6\text{Se}_7$ ),  $2 \times \sqrt{10}$  (1/6 Fe vacancies or  $\text{Fe}_5\text{Se}_6$ ), and  $\sqrt{5} \times \sqrt{5}$  (1/5 Fe vacancies or  $\text{Fe}_4\text{Se}_5$ ) mainly depend on the amount of Fe vacancies. Figs. 1d and 2c show the STM image of the  $\sqrt{5} \times \sqrt{5}$  phase, with the orientation of the

unit cell rotated  $26.6^\circ$  relative to the topmost Se lattice. It is noteworthy that all the ordered phases of Fe vacancies can only be observed with a thickness  $\geq 2$  layers, but is always absent in the monolayer case, suggesting that the site of Fe vacancies should be occupied in the van der Waals gap of FeSe–FeSe interlayer instead of the FeSe– $\text{SrTiO}_3$  interface. Also, these superstructures with varied Fe vacancies show no difference among different thicknesses, they should be bulk structures instead of only surface reconstructions.

Upon increasing the Se overflux at low temperature, more Fe vacancies are formed and the  $\sqrt{5} \times \sqrt{5}$  phase further transforms into  $\text{Fe}_3\text{Se}_4$  and  $\text{Fe}_5\text{Se}_8$ , respectively. Strategically speaking, additional interstitial Fe atoms are expected to effectively intercalate into the  $\beta$ -FeSe layers by such a low-temperature Se annealing process [48], and we can regard the  $\text{Fe}_3\text{Se}_4$  and  $\text{Fe}_5\text{Se}_8$  phase as the different levels of self-intercalation of Fe atoms within the interlayer space of the 1T-FeSe<sub>2</sub> compound. For  $\text{Fe}_3\text{Se}_4$ , while the Fe atoms along the  $b$  axis are intact, Fe vacancies are only formed along the  $a$ -axis for every two Fe rows. This leads to a  $\sqrt{3} \times 1$  reconstruction of the intercalated Fe atoms and can be reflected by the striped

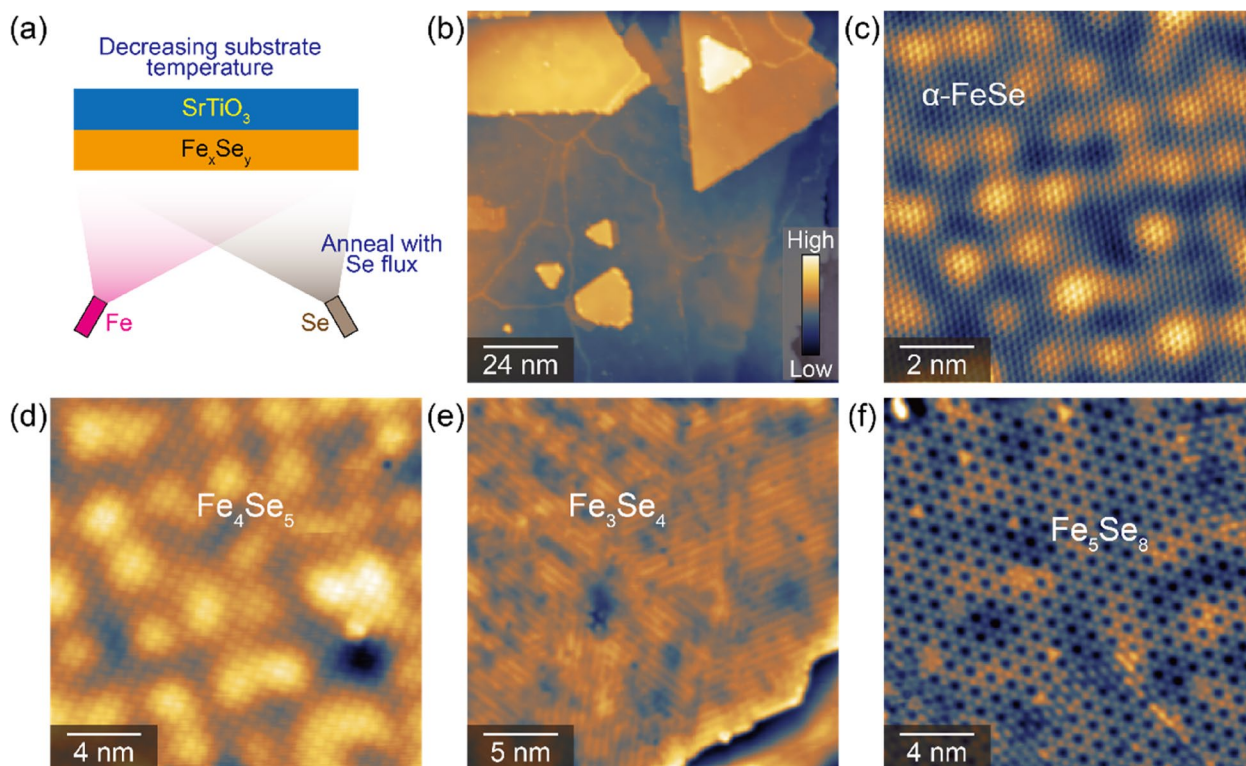


**Fig. 1** **a** Schematic illustration of the different growth conditions for different  $\text{Fe}_x\text{Se}_y$  phases by MBE. **b** Large-scale STM morphology for the  $\alpha$ -FeSe surface (scanning size:  $120 \times 120 \text{ nm}^2$ , bias voltage  $V_{\text{bias}} = +2.0 \text{ V}$ , tunneling current  $I_t = 20 \text{ pA}$ ). **c-f** Atomically resolved STM images for the  $\alpha$ -FeSe (**c**,  $10 \times 10 \text{ nm}^2$ ,  $V_{\text{bias}} = +0.05 \text{ V}$ ,  $I_t = 100 \text{ pA}$ ),  $\text{Fe}_4\text{Se}_5$  (**d**,  $20 \times 20 \text{ nm}^2$ ,  $V_{\text{bias}} = +1.0 \text{ V}$ ,  $I_t = 100 \text{ pA}$ ),  $\text{Fe}_3\text{Se}_4$  (**e**,  $25 \times 25 \text{ nm}^2$ ,  $V_{\text{bias}} = +0.5 \text{ V}$ ,  $I_t = 100 \text{ pA}$ ), and  $\text{Fe}_5\text{Se}_8$  (**f**,  $20 \times 20 \text{ nm}^2$ ,  $V_{\text{bias}} = +1.5 \text{ V}$ ,  $I_t = 100 \text{ pA}$ ) surfaces, respectively

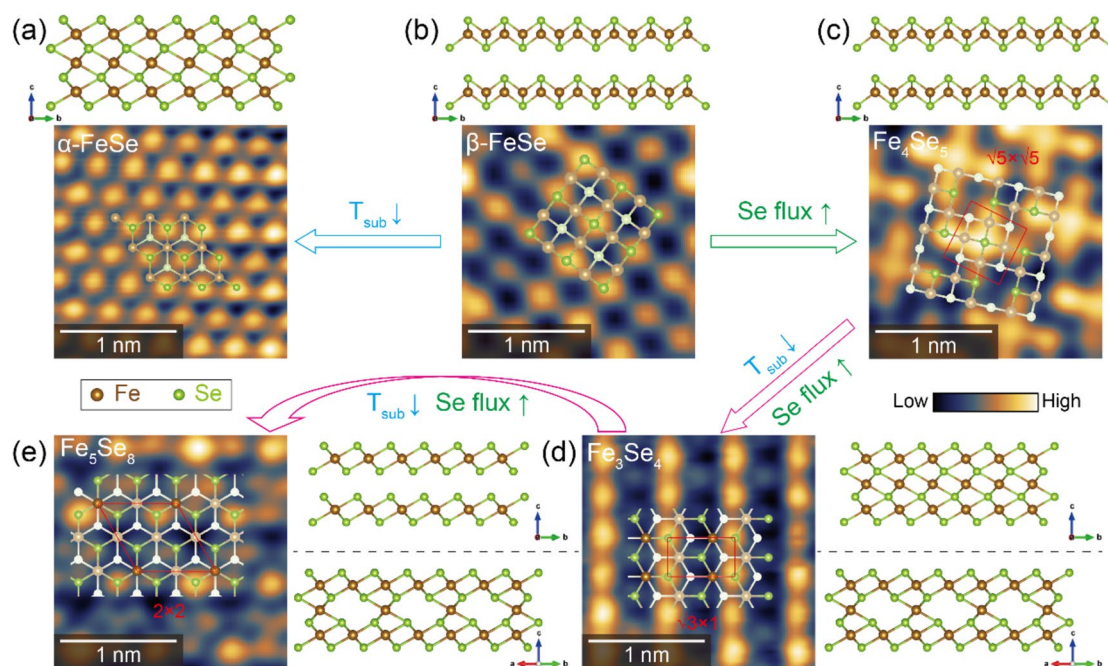


**Fig. 2** Atomically resolved STM images for different  $\text{Fe}_x\text{Se}_y$  phases grown on STO substrates under different growth conditions, respectively, for  $\alpha$ -FeSe (a),  $\beta$ -FeSe (b),  $\text{Fe}_4\text{Se}_5$  (c),  $\text{Fe}_3\text{Se}_4$  (d),  $\text{Fe}_5\text{Se}_8$  (e) surfaces, associated with their side views of crystalline structures. Their top views of toy models are also superposed onto the STM image. The red shapes stand for the unit cells of  $\sqrt{5} \times \sqrt{5}$ ,  $\sqrt{3} \times 1$ , and  $2 \times 2$  for  $\text{Fe}_4\text{Se}_5$ ,  $\text{Fe}_3\text{Se}_4$ , and  $\text{Fe}_5\text{Se}_8$ , respectively. All are acquired by  $2 \times 2 \text{ nm}^2$ ,  $V_{\text{bias}} = +0.1 \text{ V}$ ,  $I_t = 100 \text{ pA}$

**Table 1** Comparison of the stoichiometry, Fe/Se atomic ratio, STM morphology, and in-plane lattice constant of different  $\text{Fe}_x\text{Se}_y$  phases

Stoichiometry	Fe	Se	Structure	Lattice constant
$\alpha$ -FeSe	1	1	$1 \times 1$ -triangular	0.36 nm
$\beta$ -FeSe	1	1	$1 \times 1$ -squared	0.38 nm
$\text{Fe}_6\text{Se}_7$	0.86	1	$\sqrt{5} \times \sqrt{10}$ -parallelogram	$0.85 \text{ nm} \times 1.2 \text{ nm}$
$\text{Fe}_5\text{Se}_6$	0.84	1	$2 \times \sqrt{10}$ -parallelogram	$0.76 \text{ nm} \times 1.2 \text{ nm}$
$\text{Fe}_4\text{Se}_5$	0.8	1	$\sqrt{5} \times \sqrt{5}$ -squared	0.85 nm
$\text{Fe}_3\text{Se}_4$	1.5	2	$\sqrt{3} \times 1$ -striped	$0.59 \text{ nm} \times 0.34 \text{ nm}$
$\text{Fe}_5\text{Se}_8$	1.25	2	$2 \times 2$ -kagome	1.18 nm
$\text{FeSe}_2$	1	2	No intercalation	0.34 nm [49]

patterns of the topmost Se surface, as seen in Fig. 2d. For the  $\text{Fe}_5\text{Se}_8$  phase, the intercalated Fe atoms are alternatively arranged along both the  $a$  and  $b$  axes of the Fe layer, resulting in a  $2 \times 2$  pattern of kagome-like morphology (Fig. 2e). Such a kagome lattice is comprised of ordered hexagons that are interconnected by interlaced triangles, combining into arrays of corner-sharing triangles. In Table 1, we compare the crystalline properties of different  $\text{Fe}_x\text{Se}_y$  phases, including stoichiometry, Fe/Se atomic ratio, STM morphology, and in-plane lattice constant.

Overall, the growth phase strongly depends on the detailed annealing treatments with Se flux at low

temperatures. Low substrate temperature mainly drives the triangular structure of  $\alpha$ -FeSe, and the supplied Se flux provides the formation of Fe-vacancies (or intercalated Fe). These transitions are 100% with pure  $\alpha$ -FeSe and  $\text{Fe}_4\text{Se}_5$  phases. With more Fe-vacancies, the compounds  $\text{Fe}_3\text{Se}_4$  and  $\text{Fe}_5\text{Se}_8$  are formed, where the intercalation concentration strongly relies on the annealing time. Statistically, a nearly pure  $\text{Fe}_3\text{Se}_4$  phase ( $\sim 100\%$ ) can be obtained with different striped domains, as displayed in Fig. 1e. Unfortunately, with further annealing, the sample is maximumly covered by 70%  $\text{Fe}_5\text{Se}_8$  phase, whereas the other 30% regions are  $\text{Fe}_3\text{Se}_4$ . This means the efficiency of intercalating Fe atoms is limited at this stage. In the future, we hope to construct the expected  $\text{FeSe}_2$  phase with a layered structure [49] via such an intercalation strategy.

Having identified the detailed crystalline structure and STM morphologies of different  $\text{Fe}_x\text{Se}_y$  phases, we then systematically study their electronic structure by performing low-temperature STS measurements, where the  $dI/dV$  spectrum is proportional to its local density of states. Figure 3a summarizes the tunneling conductance for all the observed  $\text{Fe}_x\text{Se}_y$  phases. While  $\beta$ -FeSe is metallic (superconductive),  $\alpha$ -FeSe becomes semiconducting with a band gap of  $\sim 0.2 \text{ eV}$ . With increasing the concentration of Fe vacancies, it shows an insulating behavior with a typical gap size of  $0.5\text{--}1.0 \text{ eV}$ . When coming into

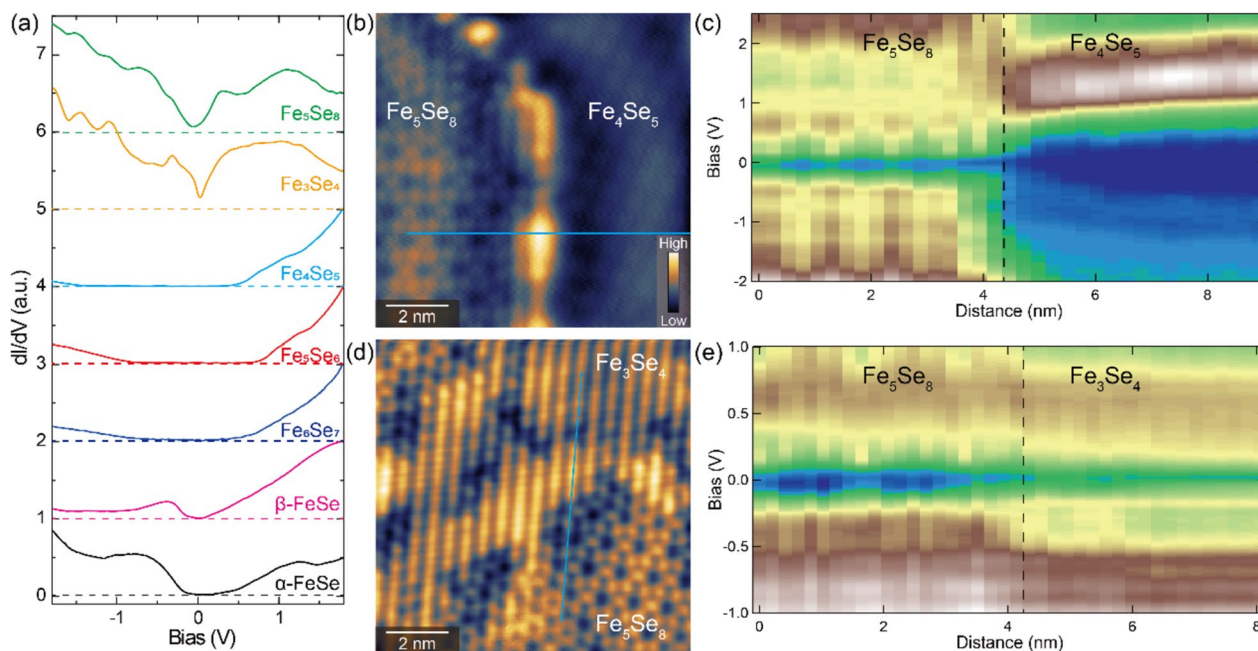


**Fig. 3** **a** STS spectra for different  $\text{Fe}_x\text{Se}_y$  phases, respectively. All spectra are shifted vertically for clarity. The dashed horizontal lines with the same colors mark the zero differential conductance for each curve. **b** STM image of a sharp boundary between  $\text{Fe}_4\text{Se}_5$  and  $\text{Fe}_5\text{Se}_8$  surfaces ( $10 \times 10 \text{ nm}^2$ ,  $V_{\text{bias}} = +0.1 \text{ V}$ ,  $I_t = 100 \text{ pA}$ ). **c** 2D plot for a series of tunneling spectra measured along the cyan line in **b**. The dashed vertical line represents the location of the phase boundary. **d** STM image of a sharp boundary between  $\text{Fe}_4\text{Se}_5$  and  $\text{Fe}_3\text{Se}_4$  surfaces ( $10 \times 10 \text{ nm}^2$ ,  $V_{\text{bias}} = +0.1 \text{ V}$ ,  $I_t = 100 \text{ pA}$ ). **e** 2D plot for a series of tunneling spectra measured along the cyan line in **d**. The dashed vertical line represents the location of the phase boundary

the intercalation regime, it turns to be metallic again, with an overall “V” shape of STS spectra. The conductance minimum located around the Fermi level may be possibly related to the preformed kagome band structure of Dirac cones [48]. Such distinct electronic properties can also be apparently compared by taking STS line cuts across the domain boundaries among different phases. As seen in Fig. 3b–e, an insulator-to-metal transition is clearly observed when the  $\sqrt{5} \times \sqrt{5}$   $\text{Fe}_4\text{Se}_5$  is partially converted into the kagome  $\text{Fe}_5\text{Se}_8$  phase. However, the increase of Fe intercalation from  $\text{Fe}_3\text{Se}_4$  to  $\text{Fe}_5\text{Se}_8$  only scarcely affects their electronic structure, namely, the metallic behavior, the overall landscape, the intensities of conductance, and the location of conductance minimum are slightly changed. This similarity of electronic structure is qualitatively in accordance with their surface consistency, where their topmost Se atoms are connected continuously, with only difference in the intercalated Fe densities of the buried Fe layers (50% for  $\text{Fe}_3\text{Se}_4$  and 25% for  $\text{Fe}_5\text{Se}_8$ ) [48].

For the insulating  $\text{Fe}_4\text{Se}_5$ , we have previously demonstrated its pair-checkerboard AFM ground state with in-plane magnetization by SP-STM measurements [47], where every  $\sqrt{5} \times \sqrt{5}$  lattice is centered by a four-Fe block with two up and two down spins that are collinear AFM aligned, as illustrated in Fig. 4a, b. Its real-space spin

contrast is featured by unidirectional stripes in the STM images, which recover as a 4-fold symmetry morphology by applying a perpendicular magnetic field larger than 1 T. Here, the tunneling current ( $I_t$ ) is the total sum of the spin-averaged tunneling current ( $I_0$ ) and spin-polarized tunneling current ( $I_{SP}$ ) expressed by  $I_t = I_0 + I_{SP}$ , where  $I_{SP}$  is sensitive to the relative spin angle ( $\varphi$ ) between the magnetization of the tip ( $P_{\text{tip}}$ ) and the sample ( $P_{\text{sample}}$ ), describing as  $I_{SP} \propto P_{\text{tip}} \cdot P_{\text{sample}} \cdot \cos\varphi$  [50]. In this way, the acquired SP-STM image strongly depends on the relative orientation of local spin for the sample and tip. In our Fe-coated W tip, the ferromagnetic (FM) tip apex is generally magnetized along the normal direction of the tip axis. Thus, it is sensitive to the in-plane component of sample magnetization ( $\varphi = 0$  or  $\pi$ ) but behaves as a nonmagnetic (NM) W tip if the spin structure orientates in the out-of-plane direction ( $\varphi = \pi/2$ ) at the surface. The orientation of  $P_{\text{tip}}$  can easily follow the direction of an external magnetic field ( $B$ ) of  $\sim 1 \text{ T}$ , tilting  $\varphi$  between in-plane and out-of-plane of the surface, while  $P_{\text{sample}}$  remains undisturbed [50]. Therefore, we can image the surface in a constant-current mode by varying an applied magnetic field: tip- and energy-dependent measurements help to differentiate the magnetic information from topography, and the local spin polarization of the sample can be determined at the atomic scale.

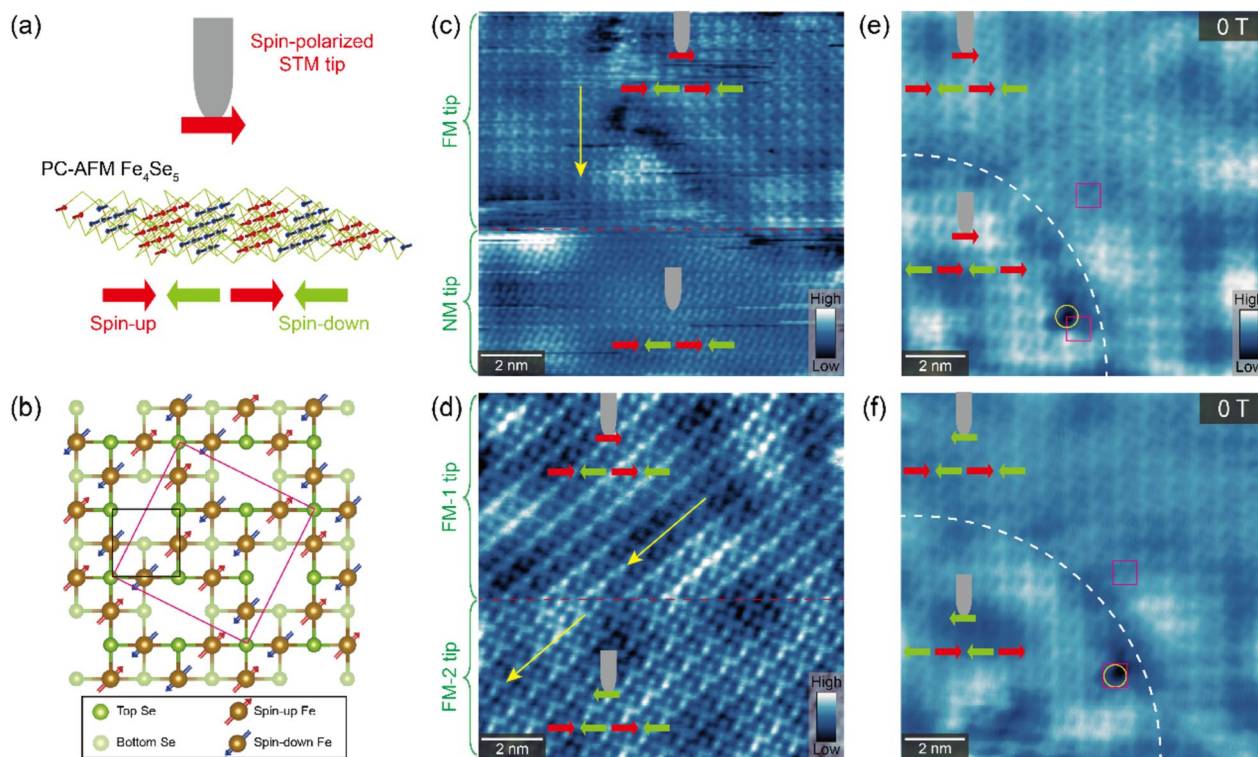


**Fig. 4** **a** Experimental schematic of SP-STM measurements on the  $\text{Fe}_4\text{Se}_5$  surface with pair-checkerboard AFM spin configuration of Fe atoms. Magnetic Fe clusters are attached at the W tip apex with in-plane spin polarization. **b** Crystal structure and magnetic order of the  $\sqrt{5} \times \sqrt{5}$  phase, whose unit cell is labeled as a magenta square. The red (blue) arrows schematically represent the ordered magnetic moments of spin up (down) on the Fe sites. **c** The FM tip suddenly loses its magnetization into an NM tip during scanning, exhibiting 4-fold symmetric patterns without stripe modulations. **d** The FM tip suddenly reverses its magnetization in the opposite direction, revealing a  $\pi$ -phase slip of the unidirectional stripes. Yellow arrows indicate the orientation of magnetic stripes. Both are acquired by  $12 \times 12 \text{ nm}^2$ ,  $V_{\text{bias}} = +1.5 \text{ V}$ ,  $I_t = 100 \text{ pA}$ ,  $B = 0 \text{ T}$ . **e, f** SP-STM images obtained by a Fe-coated W tip when ramping the magnetic field from 0 to 3 T, then backward to 0 T. The inset schematics depict the magnetization directions of the sample and tip, respectively. White dashed lines donate the domain boundaries, magenta squares stand for the  $\sqrt{5} \times \sqrt{5}$  unit cell, and the yellow circle is a defect marker for the atomic registry. All are obtained by  $10 \times 10 \text{ nm}^2$ ,  $V_{\text{bias}} = +1.5 \text{ V}$ ,  $I_t = 100 \text{ pA}$

Occasionally, due to the instability of the Fe clusters attached to the cusp of the STM tip, the FM property of the Fe-coated tip may suddenly change its spin-polarized state. Fig. 4c, d are two examples of SP-STM images by a Fe-coated W tip experiencing condition change, that is into an NM order, or reversing its magnetization in the opposite direction. As shown in Fig. 4c, the SP-STM image loses the magnetic contrast without striped features (lower half of the image). Fig. 4d is a direction comparison of opposite tip magnetization, exhibiting a  $\pi$ -phase slip of the unidirectional stripes. We note that the detailed structure of stripes varies slightly between Fig. 4c, d, mainly involving the shapes of Se atoms and their connection. This may be explained by the different shapes of Fe tips that affect the spin contrast of the topmost Se atom. However, there persists the key characteristic of field-dependent STM stripes and tip magnetization flipping under historical ramping experiences for different Fe tips. In this regard, the striped

features should stem from the magnetic properties of the sample itself, but not from the specificity of Fe tips.

The AFM domains also provide an alternative view to demonstrate its pair-checkerboard AFM configuration. Fig. 4e, f illustrate the SP-STM images comprised of two AFM domains with  $0^\circ$  boundary. It experiences a magnetic field ramp from 0 to 3 T, then backward to 0 T. A 1/2-unit-cell shift ( $\pi$ -phase slip) of the unidirectional stripes is obviously visible across the domain boundaries in Fig. 4d. Keep the defect marker (yellow circle) for atomic registry in mind, the relative position of the  $\sqrt{5} \times \sqrt{5}$  unit cell (magenta squares) exhibits a phase shift of 1/2-unit-cell along both  $a'$  and  $b'$  directions after the magnetic field cycle, while the  $\pi$ -phase slip can still be observed. This can be well understood by the relative orientations of tip and sample magnetizations, as vividly manifested by the inserted cartoons.

We also check the charge doping effect of alkali metals dosing on the AFM  $\text{Fe}_4\text{Se}_5$  surface, which has been

demonstrated as an impactful strategy to tune the superconductivity of FeSe films towards the heavily doped region [43]. As displayed in Fig. 5a–f, extra potassium (K) adatoms are introduced with different coverages and, thus different electronic doping levels. In Fig. 5g, even though the individual K atoms are randomly adsorbed, the  $dI/dV$  spectra show the homogeneously distributed insulating gap against disordered K adatoms, indicating a uniform charge doping effect. Moreover, the band gap gradually shrinks as the K coverage increases, as seen in Fig. 5h. We summarize the doping dependence of insulating gap size on the  $\text{Fe}_4\text{Se}_5$  phase in Fig. 5i. Obviously, through a wide range of electron doping to a coverage of 0.3 ML K atoms,  $\text{Fe}_4\text{Se}_5$  remains insulating with a decreased band gap by heavily doping. It had been

theoretically proposed that the  $\sqrt{5}$ -pair-checkerboard AFM state will turn into the  $\sqrt{5}$ -blocked-checkerboard AFM order (reminiscent of  $\text{K}_2\text{Fe}_4\text{Se}_5$ ) upon electron doping, meanwhile, both states keep insulating [51].

Annealing the  $\text{Fe}_4\text{Se}_5$  film can annihilate Fe vacancies, which are considered as hole dopants. Thus, the  $\text{Fe}_x\text{Se}_y$  phases with reduced Fe vacancy concentrations are equivalent to electron doping to the  $\text{Fe}_4\text{Se}_5$  films, as displayed by the decreasing band gap of other  $\text{FeSe}_x$  phases with lower Fe vacancies in Fig. 5i. Such ascription has been reported in [29], and is also collaborated from our experiments of K-doping to the  $\text{Fe}_4\text{Se}_5$  film. Unfortunately, we failed to observe the induced superconductivity with more K doping, different from what had been done in multiple-layer FeSe/SrTiO<sub>3</sub> films [15–17, 43].

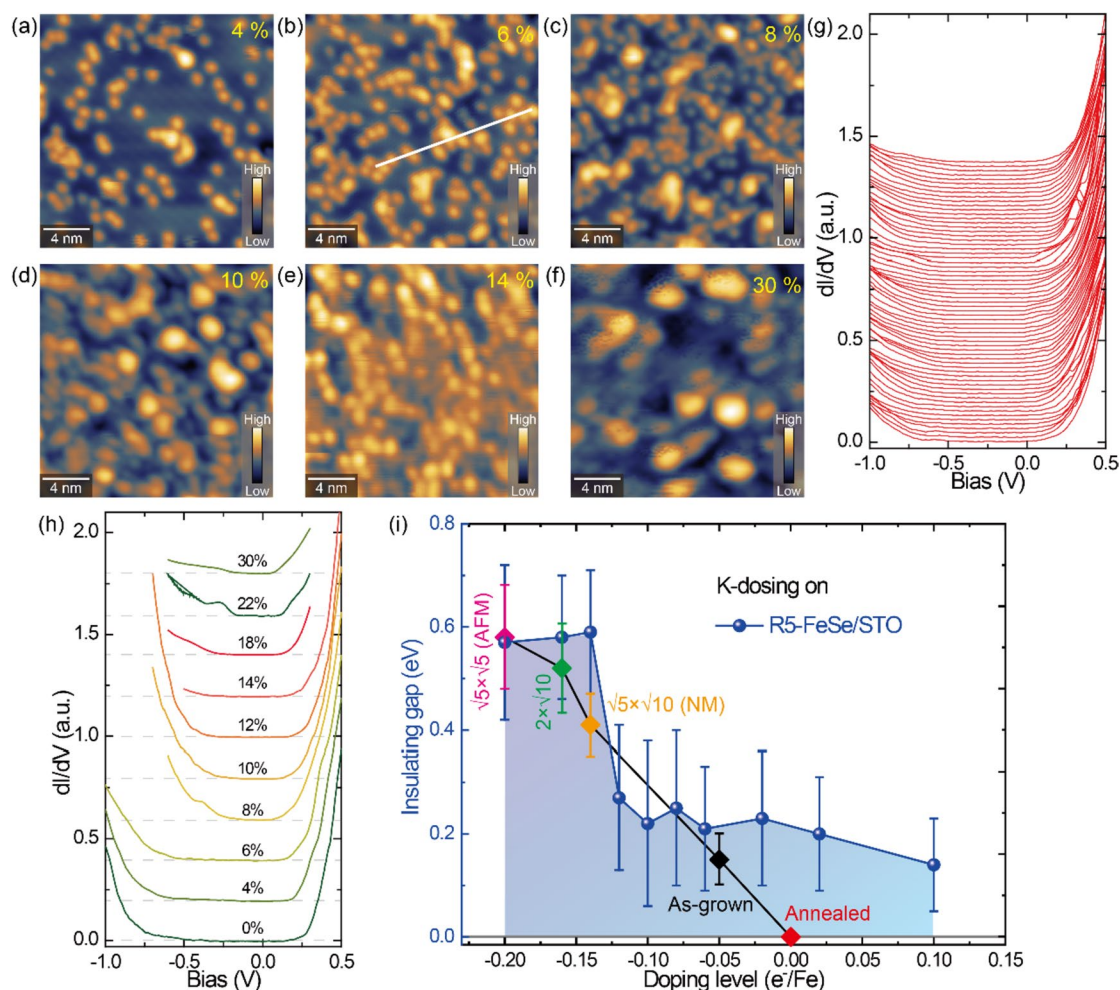


**Fig. 5** a–f STM images ( $20 \times 20 \text{ nm}^2$ ,  $V_{\text{bias}} = +2.0 \text{ V}$ ,  $I_t = 10 \text{ pA}$ ) for different surface K adsorption at various coverages: 4% (a), 6% (b), 8% (c), 10% (d), 14% (e), 30% (f), respectively. **g** Series of  $dI/dV$  spectra recorded along the white line in **b**. **h** Typical  $dI/dV$  curves taken on the K-doping  $\text{Fe}_4\text{Se}_5$  films with various doping levels as indicated. All show insulating band gaps. The horizontal broken lines mark the zero conductance for each curve. **i** Phase diagram showing the band gap sizes of  $\text{Fe}_4\text{Se}_5$  films (blue balls) under different charge doping. The error bars are statistics of 5–10 spectra at different locations. Other  $\text{FeSe}_x$  phases with different Fe vacancies are also displayed (diamond symbols, acquired from Ref. [47]) for comparison

Here, we speculate a plausible scenario as follows: Ideally, every isolated K adatom can donate a free electron to the Fe vacancies with positive charges buried underneath the topmost Se surface. However, when the K coverage grows, they tend to form clusters or islands. As such, it becomes difficult for the inner K atoms to dope electrons to the Fe vacancy layer. That is to say, it becomes difficult to achieve effective doping with increasing K for high coverage. This can be seen from the rapid decrease of gap size at low K coverage but gradually becomes saturated by adding more K adatoms.

Finally, we also carry out the STS mappings on the kagome  $\text{Fe}_5\text{Se}_8$  phase at different energies. As shown in Fig. 6a, the tunneling conductance shows a continuous evolution with increasing the bias voltage, which also delivers analogous modulations to the topographic images at each individual energy [48], suggesting a close correlation between the morphology and local density of states. These energy-dependent  $dI/dV$  mappings are further analyzed by the 2D FFT in Fig. 6b–d. By plotting the FFT intensities along the  $\Gamma\text{M}$  and  $\Gamma\text{K}$  directions, respectively, we find that the signals show nondispersive behavior of the kagome geometry in the whole energy range, well excluding the possible origin of quasiparticle interference. Moreover, the segmented FFT signals in selective energy windows, such

as  $[-0.5 \text{ V}, -0.2 \text{ V}]$ ,  $[0.05 \text{ V}, 0.25 \text{ V}]$ , and  $[0.6 \text{ V}, +1 \text{ V}]$ , suggest that the kagome effect of  $\text{Fe}_5\text{Se}_8$  phase should not be a pure structural geometry but is complicated by electronic properties.

#### 4 Conclusions

In summary, by taking full advantage of a well-controlled MBE growth process, we successfully fabricate various kinds of  $\text{Fe}_x\text{Se}_y$  phases. Their synthetic paths are summarized by the strategy of lowering substrate temperature combined with overflux Se annealing. The structural transitions and electronic properties are also systematically characterized by STM/STS measurements. While the  $\text{Fe}_5\text{Se}_8$  surface presents a kagome geometry with an electronic effect, the  $\text{Fe}_4\text{Se}_5$  phase is insulating with an AFM ground state. The spin-polarized signals are validated by the striped features, as well as its magnetic response and phase shift of adjacent domains. The surface electronic doping by K dosing is also used to balance the hole doping of Fe vacancies in  $\text{Fe}_4\text{Se}_5$ , which however is insufficient to induce superconductivity. Our work encourages to expansion of accessible atomic construction for FeSe-derived thin films, as well as exploring the close connections between magnetic stripes and charge-ordering phases crossing over the FeSe phase diagram.

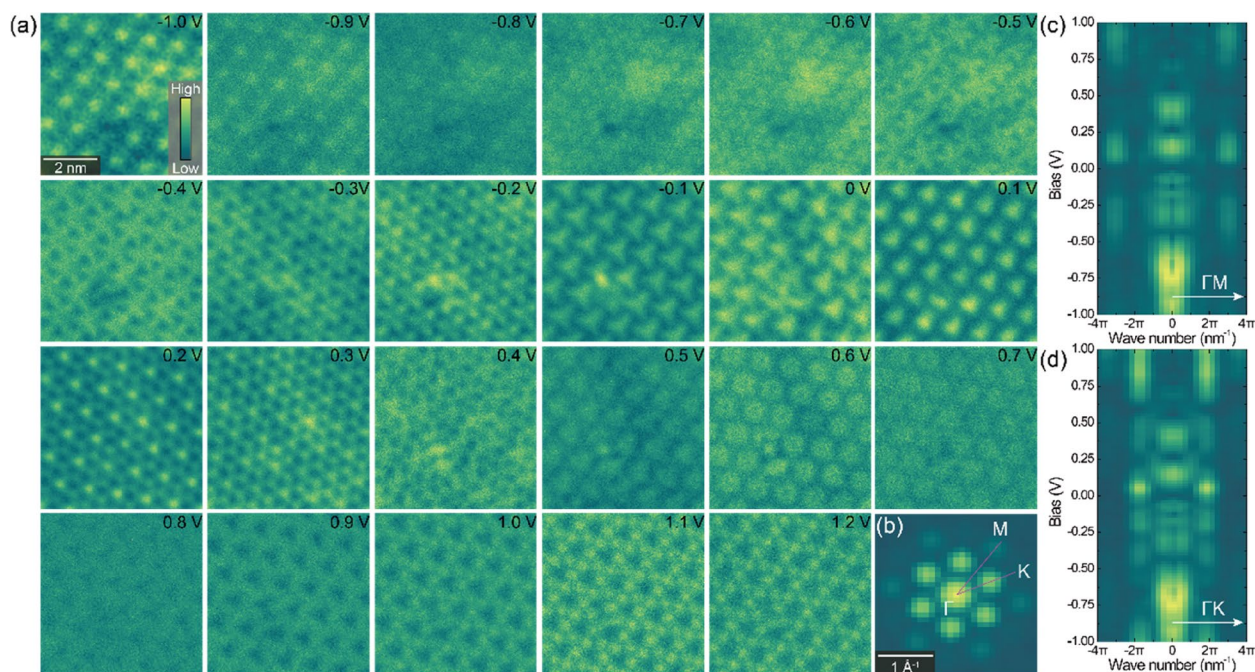


**Fig. 6** **a** A series of STS mappings acquired the  $\text{Fe}_5\text{Se}_8$  surface at different bias voltages ( $6 \times 6 \text{ nm}^2$ ,  $I_t = 100 \text{ pA}$ ). The individual energies are labeled. **b** Corresponding 2D FFT of the conductance map at 1.0 V from **a**. A 6-fold symmetrization is implemented. **c,d** 2D plot of the FFT intensities along the  $\Gamma\text{M}$  and  $\Gamma\text{K}$  directions in **b**, respectively, showing the nondispersive properties of the kagome geometry in the energy range of  $[-1 \text{ V}, +1 \text{ V}]$



### Acknowledgements

This work is funded by the National Key Research and Development Program of China (Grants No. 2022YFA1402400, 2018YFA0307000), the National Science Foundation of China (Grants No. 12174131, 92265201, U20A6002, 11774105, 11874161), the Natural Science Foundation of Hubei (2022CFB033), and Knowledge Innovation Program of Wuhan-Basic Research (2023010201010056).

### Authors' contributions

The authors contributed to all aspects of the manuscript. The authors read and approved the final manuscript.

### Funding

The National Key Research and Development Program of China (Grants No. 2022YFA1402400, 2018YFA0307000), the National Science Foundation of China (Grants No. 12174131, 92265201, U20A6002, 11774105, 11874161), the Natural Science Foundation of Hubei (2022CFB033), and Knowledge Innovation Program of Wuhan-Basic Research (2023010201010056).

### Availability of data and materials

All data and figures presented in this article are based on the materials available to the public through the corresponding references with their permissions.

### Declarations

#### Ethics approval and consent to participate

Not applicable.

#### Consent for publication

Not applicable.

#### Competing interests

The authors declare that they have no competing interests.

Received: 13 October 2023 Accepted: 16 November 2023

Published online: 27 November 2023

### References

- Q.Y. Wang et al., Interface-induced high-temperature superconductivity in single unit-cell FeSe films on SrTiO<sub>3</sub>. *Chin. Phys. Lett.* **29**, 037402 (2012)
- W.H. Zhang et al., Direct observation of high-temperature superconductivity in one-unit-cell FeSe films. *Chin. Phys. Lett.* **31**, 017401 (2014)
- J.J. Lee et al., Interfacial mode coupling as the origin of the enhancement of T<sub>c</sub> in FeSe films on SrTiO<sub>3</sub>. *Nature* **515**, 245–248 (2014)
- D. Huang, J.E. Hoffman, Monolayer FeSe on SrTiO<sub>3</sub>. *Annu. Rev. Condens. Matter Phys.* **8**, 311–336 (2017)
- D.-H. Lee, Routes to high-temperature superconductivity: a lesson from FeSe/SrTiO<sub>3</sub>. *Annu. Rev. Condens. Matter Phys.* **9**, 261–282 (2018)
- S.Y. Tan, Interface-induced superconductivity and strain-dependent spin density waves in FeSe/SrTiO<sub>3</sub> thin films. *Nat. Mater.* **12**, 634–640 (2013)
- R. Peng et al., Tuning the band structure and superconductivity in single-layer FeSe by interface engineering. *Nat. Commun.* **5**, 5044 (2014)
- R. Peng et al., Measurement of an enhanced superconducting phase and a pronounced anisotropy of the energy gap of a strained FeSe single layer in FeSe/Nb:SrTiO<sub>3</sub>/KTaO<sub>3</sub> heterostructures using photoemission spectroscopy. *Phys. Rev. Lett.* **112**, 107001 (2014)
- P. Zhang, X.-L. Peng, T. Qian, P. Richard, X. Shi, J.-Z. Ma, B.B. Fu, Y.-L. Guo, Z.Q. Han, S.C. Wang, L.L. Wang, Q.-K. Xue, J.P. Hu, Y.-J. Sun, H. Ding, Observation of high-T<sub>c</sub> superconductivity in rectangular FeSe/SrTiO<sub>3</sub>(110) monolayers. *Phys. Rev. B* **94**, 104510 (2016)
- Y.T. Cui, R.G. Moore, A.M. Zhang, Y. Tian, J.J. Lee, F.T. Schmitt, W.H. Zhang, W. Li, M. Yi, Z.K. Liu, M. Hashimoto, Y. Zhang, D.H. Lu, T.P. Devereaux, L.L. Wang, X.C. Ma, Q.M. Zhang, Q.K. Xue, D.H. Lee, Z.X. Shen, Interface ferroelectric transition near the gap-opening temperature in a single-unit-cell FeSe film grown on Nb-Doped SrTiO<sub>3</sub> substrate. *Phys. Rev. Lett.* **114**, 037002 (2015)
- H. Zhang, D. Zhang, X. Lu, C. Liu, G. Zhou, X. Ma, L. Wang, P. Jiang, Q.-K. Xue, X. Bao, Origin of charge transfer and enhanced electron-phonon coupling in single unit-cell FeSe films on SrTiO<sub>3</sub>. *Nat. Commun.* **8**, 214 (2017)
- S.-Y. Zhang, T. Wei, J.-Q. Guan, Q. Zhu, W. Qin, W.-H. Wang, J.-D. Zhang, E.W. Plummer, X.-T. Zhu, Z.-Y. Zhang, J.-D. Guo, Enhanced superconducting state in FeSe/SrTiO<sub>3</sub> by a dynamic interfacial polaron mechanism. *Phys. Rev. Lett.* **122**, 066802 (2019)
- S. He, J. He, W. Zhang, L. Zhao, D. Liu, X. Liu, D. Mou, Y.-B. Ou, Q.-Y. Wang, Z. Li, L. Wang, Y. Peng, Y. Liu, C. Chen, L. Yu, G. Liu, X. Dong, J. Zhang, C. Chen, Z. Xu et al., Phase diagram and electronic indication of high-temperature superconductivity at 65 K in single-layer FeSe films. *Nat. Mater.* **12**, 605–610 (2013)
- W.-H. Zhang, Z. Li, F.-S. Li, H.-M. Zhang, J.-P. Peng, C.-J. Tang, Q.-Y. Wang, K. He, X. Chen, L.-L. Wang, X.-C. Ma, Q.-K. Xue, Interface charge doping effects on superconductivity of single-unit-cell FeSe films on SrTiO<sub>3</sub> substrates. *Phys. Rev. B* **89**, 060506(R) (2014)
- Y. Miyata, K. Nakayama, K. Sugawara, T. Sato, T. Takahashi, High-temperature superconductivity in potassium-coated multilayer FeSe thin films. *Nat. Mater.* **14**, 775 (2015)
- J. Shiozai, Y. Ito, T. Mitsuhashi, T. Nojima, A. Tsukazaki, Electric-field-induced superconductivity in electrochemically etched ultrathin FeSe films on SrTiO<sub>3</sub> and MgO. *Nat. Phys.* **12**, 42–46 (2016)
- C.-L. Song et al., Observation of double-dome superconductivity in potassium-doped FeSe thin films. *Phys. Rev. Lett.* **116**, 157001 (2016)
- M. Yi et al., Observation of universal strong orbital-dependent correlation effects in iron chalcogenides. *Nat. Commun.* **6**, 7777 (2015)
- Q. Fan, W.H. Zhang, X. Liu, Y.J. Yan, M.Q. Ren, R. Peng, H.C. Xu, B.P. Xie, J.P. Hu, T. Zhang, D.L. Feng, Plain s-wave superconductivity in single-layer FeSe on SrTiO<sub>3</sub> probed by scanning tunnelling microscopy. *Nat. Phys.* **11**, 946–952 (2015)
- Y. Zhang, J.J. Lee, R.G. Moore, W. Li, M. Yi, M. Hashimoto, D.H. Lu, T.P. Devereaux, D.-H. Lee, Z.-X. Shen, Superconducting gap anisotropy in monolayer FeSe thin film. *Phys. Rev. Lett.* **117**, 117001 (2016)
- Z. Ge, C. Yan, H. Zhang, D. Agterberg, M. Weinert, L. Li, Evidence for d-wave superconductivity in single layer FeSe/SrTiO<sub>3</sub> probed by quasiparticle scattering off step edges. *Nano Lett.* **19**, 2497–2502 (2019)
- H. Zhang, Z. Ge, M. Weinert, and Lian Li, Sign changing pairing in single layer FeSe/SrTiO<sub>3</sub> revealed by nonmagnetic impurity bound states. *Commun. Phys.* **3**, 75 (2020)
- Y.-Y. Xiang, F. Wang, D. Wang, Q.-H. Wang, D.-H. Lee, *Phys. Rev. B* **86**, 134508 (2012)
- A. Aperis, P.M. Oppeneer, Multiband full-bandwidth anisotropic Eliashberg theory of interfacial electron-phonon coupling and high-T<sub>c</sub> superconductivity in FeSe/SrTiO<sub>3</sub>. *Phys. Rev. B* **97**, 060501(R) (2018)
- B.D. Faeth, Interfacial electron-phonon coupling constants extracted from intrinsic replica bands in monolayer FeSe/SrTiO<sub>3</sub>. *Phys. Rev. Lett.* **127**, 016803 (2021)
- B.L. Kang, M.Z. Shi, S.J. Li, H.H. Wang, Q. Zhang, D. Zhao, J. Li, D.W. Song, L.X. Zheng, L.P. Nie, T. Wu, X.H. Chen, Preformed Cooper pairs in layered FeSe-based superconductors. *Phys. Rev. Lett.* **125**, 097003 (2020)
- Y. Xu et al., Spectroscopic evidence of superconductivity pairing at 83 K in single-layer FeSe/SrTiO<sub>3</sub> films. *Nat. Commun.* **12**, 2840 (2021)
- B.D. Faeth, S.-L. Yang, J.K. Kawasaki, J.N. Nelson, P. Mishra, C.T. Parzyck, C. Li, D.G. Schlom, K.M. Shen, Incoherent Cooper pairing and pseudogap behavior in single-layer FeSe/SrTiO<sub>3</sub>. *Phys. Rev. X* **11**, 021054 (2021)
- T.K. Chen, C.C. Chang, H.H. Chang, A.H. Fang, C.H. Wang, W.H. Chao, C.M. Tseng, Y.C. Lee, Y.R. Wu, M.H. Wen, H.Y. Tang, F.R. Chen, M.J. Wang, M.K. Wu, D.V. Dyck, Fe-vacancy order and superconductivity in tetragonal β-Fe<sub>1-x</sub>Se. *Proc. Natl. Acad. Sci. U.S.A.* **111**, 63 (2014)
- K.-Y. Yeh, T.-S. Lo, P.M. Wu, K.-S. Chang-Liao, M.-J. Wang, M.-K. Wu, Magnetotransport studies of Fe vacancy-ordered Fe<sub>4+δ</sub>Se<sub>5</sub> nanowires. *Proc. Natl. Acad. Sci. U. S. A.* **117**, 12606 (2020)
- Y. Hu et al., Discovery of an insulating parent phase in single-layer FeSe/SrTiO<sub>3</sub> films. *Phys. Rev. B* **102**, 115144 (2020)
- F. Ye, S. Chi, W. Bao, X.F. Wang, J.J. Ying, X.H. Chen, H.D. Wang, C.H. Dong, M. Fang, Common crystalline and magnetic structure of superconducting A<sub>2</sub>Fe<sub>4</sub>Se<sub>5</sub> (A=K, Rb, Cs, Tl) single crystals measured using neutron diffraction. *Phys. Rev. Lett.* **107**, 137003 (2011)

33. W. Bao, Q.-Z. Huang, G.-F. Chen, D.-M. Wang, J.-B. He, Y.-M. Qiu, A novel large moment antiferromagnetic order in  $K_{0.8}Fe_{1.6}Se_2$  superconductor. *Chin. Phys. Lett.* **28**, 086104 (2011)
34. D. Liu et al., Common electronic features and electronic nematicity in parent compounds of iron-based superconductors and FeSe/SrTiO<sub>3</sub> films revealed by angle-resolved photoemission spectroscopy. *Chin. Phys. Lett.* **33**, 077402 (2016)
35. B. Lei, J.H. Cui, Z.J. Xiang, C. Shang, N.Z. Wang, G.J. Ye, X.G. Luo, T. Wu, Z. Sun, X.H. Chen, Evolution of high-temperature superconductivity from a low-T<sub>c</sub> phase tuned by carrier concentration in FeSe thin flakes. *Phys. Rev. Lett.* **116**, 077002 (2016)
36. M. Burrard-Lucas, D.G. Free, S.J. Sedlmaier, J.D. Wright, S.J. Cassidy, Y. Hara, A.J. Corkett, T. Lancaster, P.J. Baker, S.J. Blundell, S.J. Clarke, Enhancement of the superconducting transition temperature of FeSe by intercalation of a molecular spacer layer. *Nat. Mater.* **12**, 15–19 (2013)
37. X.F. Lu, N.Z. Wang, H. Wu, Y.P. Wu, D. Zhao, X.Z. Zeng, X.G. Luo, T. Wu, W. Bao, G.H. Zhang, F.Q. Huang, Q.Z. Huang, X.H. Chen, Coexistence of superconductivity and antiferromagnetism in  $(Li_{0.8}Fe_{0.2})OHFeSe$ . *Nat. Mater.* **14**, 325–329 (2015)
38. M.Z. Shi, N.Z. Wang, B. Lei, C. Shang, F.B. Meng, L.K. Ma, F.X. Zhang, D.Z. Kuang, X.H. Chen, Organic-ion-intercalated FeSe-based superconductors. *Phys. Rev. Mater.* **2**, 074801 (2018)
39. Z. Zhang, M. Cai, R. Li, F. Meng, Q. Zhang, L. Gu, Z. Ye, G. Xu, Y.-S. Fu, W. Zhang, Controllable synthesis and electronic structure characterization of multiple phases of iron telluride thin films. *Phys. Rev. Mater.* **4**, 125003 (2020)
40. X.-Q. Yu, M.-Q. Ren, Y.-M. Zhang, J.-Q. Fan, S. Han, C.-L. Song, X.-C. Ma, Q.-K. Xue, Stoichiometry and defect superstructures in epitaxial FeSe films on SrTiO<sub>3</sub>. *Phys. Rev. Mater.* **4**, 051402(R) (2020)
41. J.-Q. Guan, L. Wang, P. Wang, W. Ren, S. Lu, R. Huang, F. Li, C.-L. Song, X.-C. Ma, Q.-K. Xue, Honeycomb lattice in metal-rich chalcogenide Fe<sub>2</sub>Te. *Chinese Phys. Lett.* **38**, 116801 (2021)
42. Z. Zhang, Y. Yuan, W. Zhou, C. Chen, S. Yuan, H. Zeng, Y.-S. Fu, W. Zhang, Strain-induced bandgap enhancement of InSe ultrathin films with self-formed two-dimensional electron gas. *ACS Nano* **15**, 10700–10709 (2021)
43. W.H. Zhang, X. Liu, C.H.P. Wen, R. Peng, S.Y. Tan, B.P. Xie, T. Zhang, D.L. Feng, Effects of surface electron doping and substrate on the superconductivity of epitaxial FeSe films. *Nano Lett.* **16**, 1969–1973 (2016)
44. H. Xia, Y. Li, M. Cai, L. Qin, N. Zou, L. Peng, W. Duan, Y. Xu, W. Zhang, Y.-S. Fu, Dimensional crossover and topological phase transition in Dirac semimetal Na<sub>3</sub>Bi films. *ACS Nano* **13**, 9647–9654 (2019)
45. L. Peng, J. Qiao, J.-J. Xian, Y. Pan, W. Ji, W. Zhang, Y.-S. Fu, Unusual electronic states and superconducting proximity effect of Bi films modulated by a NbSe<sub>2</sub> substrate. *ACS Nano* **13**, 1885–1892 (2019)
46. J.-J. Xian, C. Wang, J.-H. Nie, R. Li, M. Han, J. Lin, W.-H. Zhang, Z.-Y. Liu, Z.-M. Zhang, M.-P. Miao, Y. Yi, S. Wu, X. Chen, J. Han, Z. Xia, W. Ji, Y.-S. Fu, Spin mapping of intralayer antiferromagnetism and field-induced spin reorientation in monolayer CrTe<sub>2</sub>. *Nat. Commun.* **13**, 257 (2022)
47. W. Zhang, Z.-M. Zhang, J.-H. Nie, B.-C. Gong, M. Cai, K. Liu, Z.-Y. Lu, Y.-S. Fu, Spin-resolved imaging of antiferromagnetic order in Fe<sub>4</sub>Se<sub>5</sub> ultrathin films on SrTiO<sub>3</sub>. *Adv. Mater.* **35**, 2209931 (2023)
48. Z.-M. Zhang, B.-C. Gong, J.-H. Nie, F. Meng, Q. Zhang, L. Gu, K. Liu, Z.-Y. Lu, Y.-S. Fu, W. Zhang, Self-Intercalated 1T-FeSe<sub>2</sub> as an Effective Kagome Lattice. *Nano Lett.* **23**, 954–961 (2023)
49. H. Liu, Y. Xue Van, Der Waals epitaxial growth and phase transition of layered FeSe<sub>2</sub> Nanocrystals. *Adv. Mater.* **33**, 20084 (2021).
50. R. Wiesendanger, Spin mapping at the nanoscale and atomic scale. *Rev. Mod. Phys.* **81**, 1495 (2009)
51. M. Gao, X. Kong, X.-W. Yan, Z.-Y. Lu, T. Xiang, Pair-checkerboard antiferromagnetic order in  $\beta$ -Fe<sub>4</sub>Se<sub>5</sub> with  $\sqrt{5}\times\sqrt{5}$ -ordered Fe vacancies. *Phys. Rev. B* **95**, 174523 (2017)

## Publisher's Note

Springer Nature remains neutral with regard to jurisdictional claims in published maps and institutional affiliations.